Mechanical behavior of an altered reservoir limestone: multi-scale and core analysis approaches

Louis Zinsmeister[1-2], Jérémie Dautriat[1], Nicolas Gland[1], Alexandre Dimanov[2] Michel Bornert[3] and Jean Raphanel[2].

(1) IFP Energies Nouvelles – 1 & 4 avenue du Bois-Préau – 92852 Rueil-Malmaison Cedex - France

(2) Laboratoire de Mécanique des Solides –UMR CNRS 7649 - Ecole Polytechnique – 91128 Palaiseau Cedex - France

(3) Laboratoire Navier – UMR CNRS 8205 - Ecole des Ponts ParisTech - 6 & 8 avenue Blaise Pascal – 77455 Champs sur Marne Cedex 2 - France

This paper was prepared for presentation at the International Symposium of the Society of Core Analysts held in Scotland, UK, 27-30 August, 2012

ABSTRACT

The success of CO_2 geological storage requires the insurance of long term injectivity and integrity over the site. In contrary to conventional hydrocarbon gas injection, CO_2 injection may induce geochemical reactions between the reactive brine and the host rock, leading to modifications of petrophysical and geomechanical properties. This study aims to relate the evolution of these properties to the chemically-induced microstructural evolution by multi-scale characterization. Classical laboratory procedures of co-injecting supercritical CO_2 and brine or brine saturated with CO_2 lead to wormholing and heterogeneous dissolution patterns, which makes difficult the measurements at the plug scale. In the present study carbonate samples have been subjected to Retarded Acid Treatments (RAT). This protocol mimics the effects of long-term alteration mechanisms, by insuring a homogeneous dissolution pattern throughout the samples. Porosity, permeability and mechanical properties are measured and compared between intact and successively altered samples. The effects of alteration on these properties are discussed in terms of microstructural evolution, based on classical core analysis (NMR and Hg-Porosimetry), thin-section observations and Scanning Electron Microscopy (SEM). The evolutions of mechanical properties are studied by conventional triaxial tests, which show a weakening of the samples with the alteration. This weakening may be first related to the increase of the sample porosity. However, other microstructural changes may be involved as well. Therefore a quantitative and continuous micro-mechanical investigation is needed to define more precisely the history and the localization of the deformation during compression. Full-field measurement techniques combining in-situ observations and Digital Image Correlation (DIC) are the best suited techniques for this purpose. Sequences of optical and SEM images have been acquired on respectively macroscopic and centimetric samples during uniaxial compressive loading and treated by DIC. Homogeneous deformation is observed on intact samples while it is localized in altered ones. The integrated and multi-scale approach proposed in this paper, combining classical petrophysical and original

geomechanical measurements, will contribute to the development of micro-mechanically based constitutive laws for implementation in geomechanical reactive transport simulators.

INTRODUCTION

CO_2 injection in deep aquifer is a promising technique developed to reduce the greenhouse effect, but it may affect the reservoir integrity and cause leakage. Dissolution is one of the processes induced by the CO_2 injection; dissolution patterns vary with the distance to the injection well [1]. Next to the well, heterogeneous alteration is observed and a lot of studies have been made to determine its impact on mechanical [2] and flow [3,4] property evolutions. This paper focuses on the homogeneous alteration case. First studies using a retarded acid treatment (RAT) in order to mimic a homogeneous alteration [5,6] show a stronger decrease of the elastic moduli than expected from classical poromechanical models [7,8]. Dautriat *et al.* [9] applied the Digital Image Correlation (DIC) method on heterogeneous intact Estaillades limestone and successfully determined specific micromechanical behaviors like micro-crack opening. Based on these different methods, our study uses the RAT protocol and integrates most of the classical petrophysical methods, applied at macro, meso and micro scales in order to characterize the effects of alteration. The study is completed with DIC of optical and Scanning Electron Microscopy (SEM) imaging during uniaxial loading.

INTACT ROCK CHARACTERIZATION

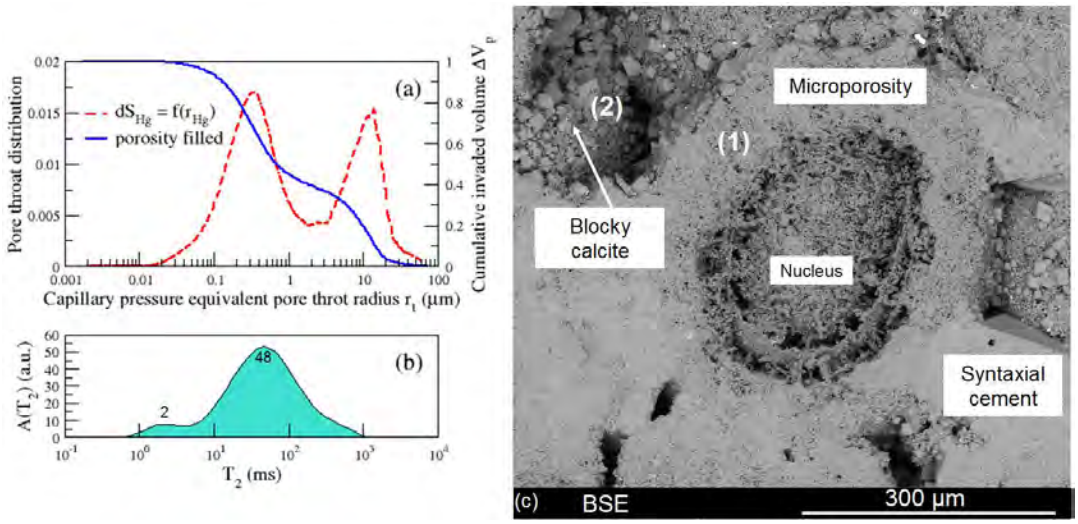

Figure 1 : (a) Pore throats distribution obtained by Hg-porosimetry, (b) NMR T2 relaxation times distribution and (c) microstructures of the Lavoux limestone imaged by SEM : (1) indicates the microporosity within the oolites, (2) indicates the inter-grains macroporosity

The studied rock comes from the Lavoux limestone quarry located in the vicinity of Poitiers in France. This material is a nearly pure calcite oolitic limestone formed in a strong and continuous rolling flow environment. Three main structures are observed by SEM (Fig. 1(c)), microporous and rounded oolites with an average size of 500 µm, large syntaxial cements and small rhombohedra calcite cement at the boundaries of the oolites.

In order to describe the porous network, classical petrophysical measurements have been performed, such as Scanner Tomography, High Pressure Mercury Injection (HPMI), Nuclear Magnetic Resonance (NMR) and porosity estimation by dry and wet weights. The porosity is bimodal (as shown by NMR T2 distribution in Fig. 1(b)) with a large macroporosity (inter-grains) and a smaller microporosity within the oolites (intra-grains) having mean pore throat radii of 11 µm and 0.3 µm, respectively (HPMI in Fig. 1(a)). The porosity measured by dry and wet weights ranges from 20% to 26% for a mean value of 24%. For alteration and mechanical tests, 80 mm x 40 mm cylindrical core samples have been selected with respect to a mean porosity close to 24% ±0.5%, and a homogeneous porosity along the sample length, as revealed by CT-scanner imaging. In spite of this selection, the permeability ranges from 85 mD to 140 mD for seven samples.

HOMOGENEOUS ALTERATION

Protocol

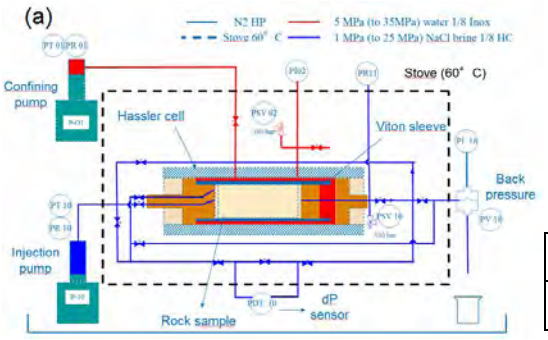

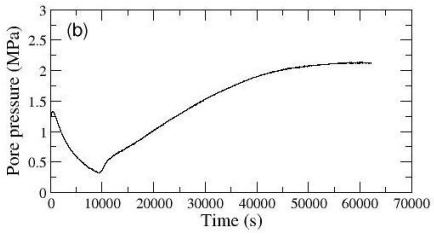

P_{conf} (MPa)	P_{pore} (MPa)	Temp. (°C)	Alteration time	Saturated fluid
6	1	60	~ 12 h	brine NaCl 5 g/L

Figure 2 : (a) Upgraded experimental set-up for alteration and brine permeability measurements, (b) pore pressure evolution during the alteration. The experimental conditions are reported in the table

The sample alteration technique is based on RAT following the protocol described by Egermann *et al.* [5], we recall that RAT insures a homogeneous alteration unlike conventional CO_2-brine injection experiments [3,4]. The experimental set-up (Fig. 2(a)) is composed of a confining Hassler cell, which allows the application of a hydrostatic stress on the sample, which is isolated from the confining medium by a core sleeve. The intact state permeability is measured at a confining pressure of Pc = 6 MPa. Afterwards, the brine is flushed out by the injection of three pore volumes (V_p) of an initially inactive acid. The sample is then placed under undrained conditions and the temperature is increased to 60°C to activate the acid. When the pore pressure reaches a plateau (usually after one night, see Fig. 2(a)), the equilibrium between reactive fluid and carbonate is assumed, and the core is flushed by fresh brine. Effluents are collected and the particle size distribution is measured by laser diffraction. The complete protocol is repeated until a chosen porosity increase is reached. Permeability is measured between each RAT. Finally, the dried sample is imaged by a medical scanner, to check the homogeneity of the alteration and estimate the porosity increase. The experimental set-up has been upgraded to allow the measurement of the permeability in opposite directions, to evaluate the impact of potential fine particles mobilization in the porous network.

Petrophysical and Microstructural Evolutions

Petrophysical Changes

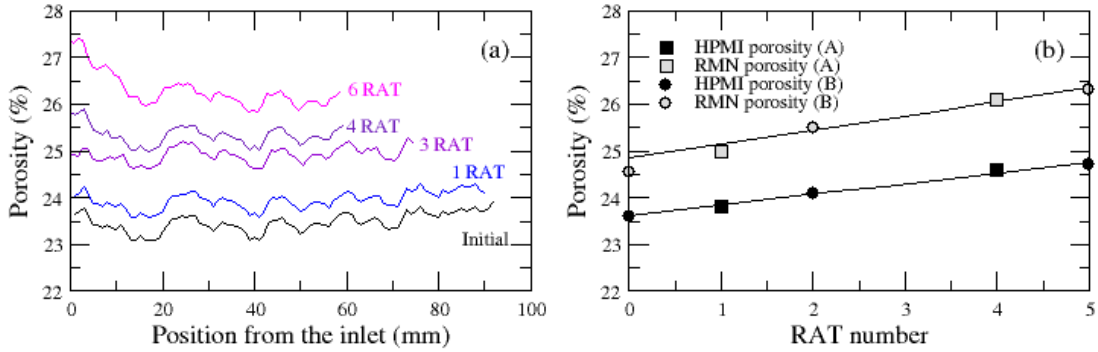

Figure 3 : (a) Typical evolution of the porosity profile of sample A subjected to successive RATs measured by X-ray scanner, (b) porosity evolution with RAT number obtained by MNR and HPMI on two samples A and B

Fig. 3(a) presents the porosity profiles obtained from CT-scanner analyses performed at successive RATs on sample A. After each cycle, a slice of the sample is cut for HPMI and MNR analyses and for thin sections preparation. The evolution of profiles showed a conservation of initial local heterogeneity of porosity and a constant increase of mean porosity for each RAT. Only the inlet part appeared more heterogeneously altered, probably due to an exceeding concentration of acid in the piston groove. To avoid a potential effect of this more altered region, 5 mm of material are removed when preparing samples for mechanical tests. Fig. 3(b) shows the evolution of porosity measured by HPMI and MNR on two different samples (A and B). The discrepancy between the porosity values obtained by the two methods is a well known phenomenon. It could be explained by a microstructural crushing at High Pressure of Hg injection, which can lead to a closure of smaller pores. Nevertheless, the two methods showed the same linear porosity increase of 0.2 p.u/RAT with NMR and HPMI (on 15 mm x 17 mm core) for a 10% diluted acid.

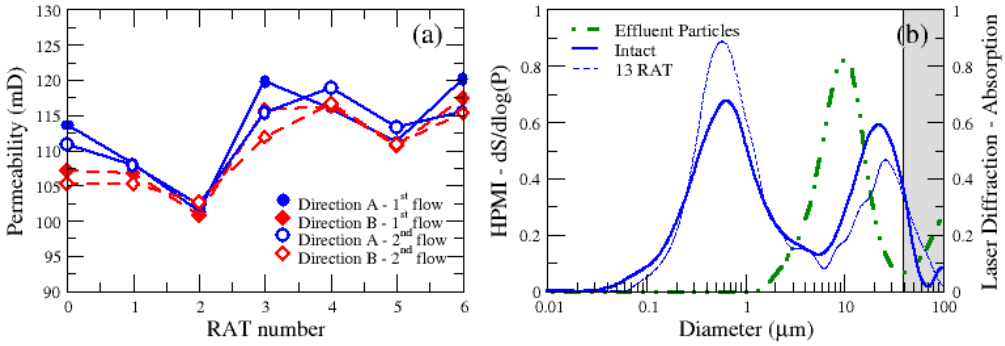

Figure 4 : (a) Permeability evolution with the alteration and for two directions of measurement (b) outgoing particles and pore throat evolution after 13 cycles of alteration obtained by HPMI and laser diffraction

The permeability evolution was more complex, as shown in Fig. 4(a). To avoid potential effects of sample cut, the presented permeability measurements have been performed on a

same 80 mm x 40 mm core maintained in the cell between each RAT. The permeability evolution presented cyclic evolution with successive phases of increase and reduction, without evidence of an important impact of the measurement direction for a same alteration state. As shown in Fig. 4(b), an increase of the proportion of micropore throat and a spreading of the macropore throats distribution are observed, which suggest a permeability increase. The superimposed curve of effluent particles in Fig. 4(b) evidences however the existence of outgoing particles, which a range of diameters from a few micrometers (micrograins of calcite constitutive of oolites) to a few tens of micrometers (macropore throats sizes). We cannot exclude that larger mobilized particles remain stuck in the porosity, which will decrease the permeability.

Microstructural Changes

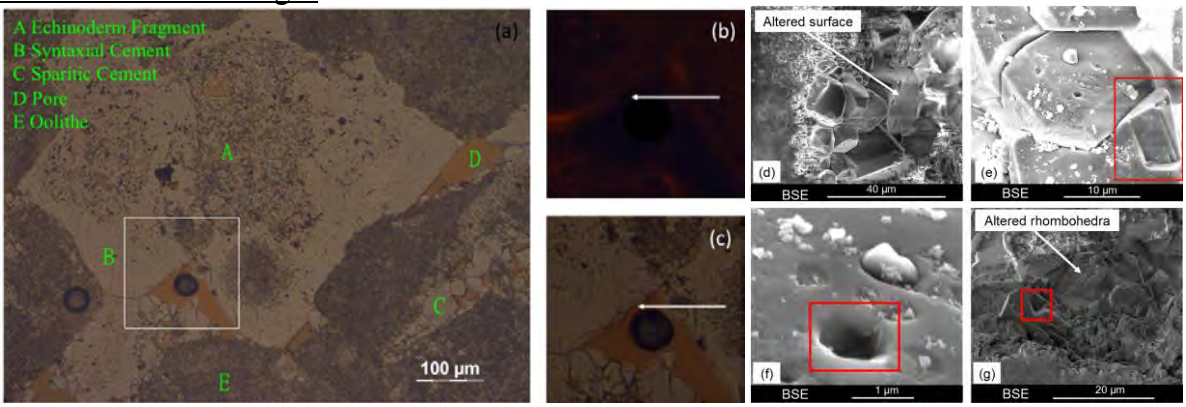

Figure 5 : (a) Thin section of the Lavoux limestone after 13 RATs, focus on alteration patterns on the syntaxial cement surface imaged by (b) cathodoluminescence and (c) white light and SEM observations of corrosion pits at the calcite rhomobohedra surface obtained after (d,e,f) 2 RATs and (g) 13 RATs

The impacts of alteration on the microstructure have been investigated by thin sections and SEM imaging. For this purpose, a high number (13) of RATs has been performed on a sample to enhance the alteration effect. Corrosion pits on calcite rhombohedra are observed (Fig. 5(d,e) and dissolution patterns are observed on syntaxial cement under white light and cathodoluminescence (Fig. 5(a,b,c)). Some cements showed the imprint of missing imbricated crystals, possibly due to a loss of cohesion between cement grains induced by alteration (Fig. 5(e,f,g)). These torn out particles are probably responsible for clogging of macropore throats. The 13 RAT sample showed a pyramidal dissolution pattern of small calcite cements (Fig. 5(g)), which can be explained by the alteration of crystalline planes of the rhombohedra.

Because of post-mortem imaging, we are only able to identify the micromechanisms of dissolution on well-defined structures such as cements. Nevertheless, these local mechanisms are probably not the only cause of the mean porosity increase and an effect of alteration on oolites is also expected. A comparative analysis of a sample imaged by 3D micro-tomography at successive RATs is in progress to estimate the increase of porosity related to microporous oolites alteration.

Mechanical Behavior and Weakening Effect

Confining Pressure (MPa)	6	11	16
X-ray porosity (%)	24.4	24.1	24.1
E (GPa)	17.8	21.8	22.1
v	0.25	0.23	0.2
Effective failure (MPa)	32.4	37.8	38.0

	Intact	Altered 3x
X-ray porosity (%)	24.3	24.4
E (GPa)	23	12
v	0.2	0.19
UCS (MPa)	33.8	18.3

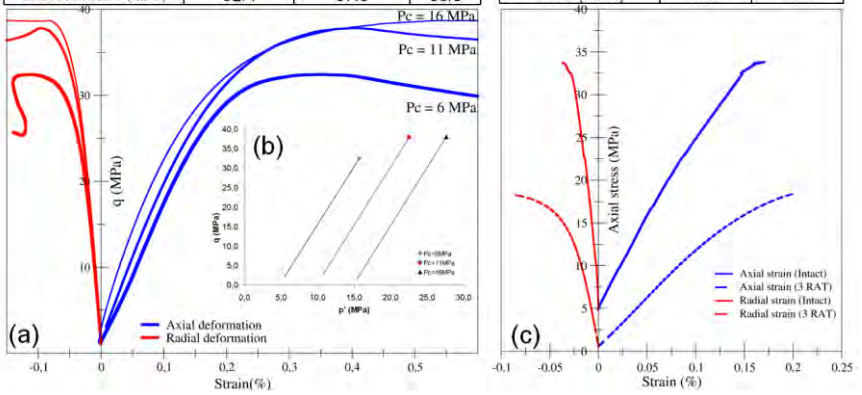

Figure 6 : (a) Stress-strain curves obtained on intact samples at different confining pressures and (b) associated critical stress reported in the p'-q (mean effective pressure-deviatoric stress) diagram, (c) stress-strain curves obtained on intact and 3 RATs samples loaded uniaxially

During triaxial tests, the axial force, and the pore and the confining pressures are monitored. Axial and radial deformations are measured by strain gauges glued on the sample circumference. Each sample is saturated with mineral oil and the pore pressure maintained constant at Pp = 1 MPa. A first drained triaxial loading is performed at low confining pressure (Pc = 2 MPa) to determine the elastic moduli. The mean Young's modulus and Poisson's ratio of the Lavoux limestone are respectively 20.6 GPa and 0.24. The sample is then hydrostatically loaded up to a chosen pressure. Once this pressure is reached, the axial stress is increased until sample failure. Three confining pressures (6 MPa, 11 MPa and 16 MPa) are used in order to determine the brittle regime limit (Fig. 6(a)). At the lower confining pressures a peak stress is observed (brittle regime) while at Pc = 16 MPa, a transition regime involving shear enhanced compaction mechanisms is reached [10].

Fig. 6(b) shows the strain evolutions of intact and after 3 RATs wet samples under simple compression. Despite the same porosity for the two samples, we observed a strong weakening of the rock, resulting in a decrease of Young's modulus from 23.6 to 11.8 GPa and of the Uniaxial Compressive Strength (UCS) from 33.8 to 18.3 MPa. This observation indicates that the increase in porosity is not the unique parameter governing the mechanical behavior of the altered material. The loss of solid matrix (micrite and cement) cohesion may also play a part.

DIGITAL IMAGE CORRELATION

Methodology of Digital Image Correlation

In this study, the full-field measurements include the acquisition of pictures of the surface of a sample subjected to simple compressive loading. The DIC method allows the determination of the displacement field and the calculation of the associated strain field at successive stages of loading [11, 12]. For this purpose, a reference 'undeformed' image is

discretized into a grid of regularly spaced points. A correlation domain D is devoted to each grid point of index i. The DIC procedure consists in identifying the similar domain of the 'deformed' images, homologous to the ones of the reference image, by minimizing a correlation function C [11]:

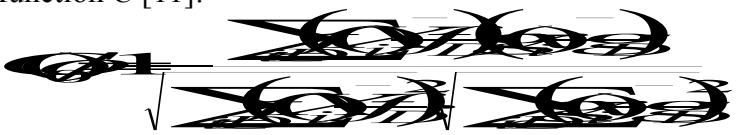

(1)

where X_i and x_i are the coordinates of similar points in the reference image and in the deformed one, which are associated by an approximation of the mechanical transformation ϕ_0, minimizing C. $f(X_i)$ and $g(x_i)$ are respectively the grey levels of point i in the reference image and in the deformed image; f_D and g_D are respectively the averages of the grey levels on the domain D and on the homologous domain transformed by ϕ_0. A subpixel resolution on the displacement is obtained by a bilinear interpolation of the grey level in each domain. The coordinates of the homologous domain centers provide the displacement field, which allows the computation of in-plane strain components (ε_{11}, ε_{22}, ε_{12}) by a contour integration on a chosen area. The size of this area ranges from the complete studied grid, providing global strain measurements, to nearest neighbour points of each point of the grid providing a local strain. The magnitude of the component of this strain field may be represented by colours levels superimposed on the microstructure images. One may also plot the equivalent strain that von Mises expressed by (2) under the assumption of axisymmetry:

(2)

Experimental set-up

The DIC study has been performed at two scales on macroscopic samples imaged by optical devices and high resolution camera, and on small samples imaged by SEM.

The macroscopic compression tests are performed on a vertical loading frame controlled in displacement. Cylindrical samples of 37 mm high and 36 mm in diameter are machined in order to produce two opposite flattened 25 mm wide surfaces. The applied load and displacement are measured by a force sensor and a LVDT. A constant displacement rate of 1 µm/s is imposed until sample failure. During loading, images of one flattened surface are taken at constant time intervals by a high resolution CCD camera (4872x3248 ~16 Mpixel) covering the whole surface (with pixel size ~7 µm). Black and white painting sprays are applied to enhance local contrast and optimize the DIC efficiency.

Small parallelepiped samples (14 mm x 7 mm) are tested inside a SEM equipped with a simple compression rig (maximum load 5 kN). Displacement is controlled at a rate of ~1 µm/s. The SEM image acquisition lasts several minutes, consequently the loading is performed in a stepwise manner. The natural contrast of the material is sufficient for DIC, but the contrast and brightness must be optimized before each acquisition to spread the grey level histogram over the full 16 bit range. The magnification varies from x60 to x80, corresponding to imaged surfaces of 2.1mm x 1.8mm (5 µm of resolution) and 1.6 mm x 1.4 mm (3.9 µm of resolution).

Large Scale Effects Of The Alteration

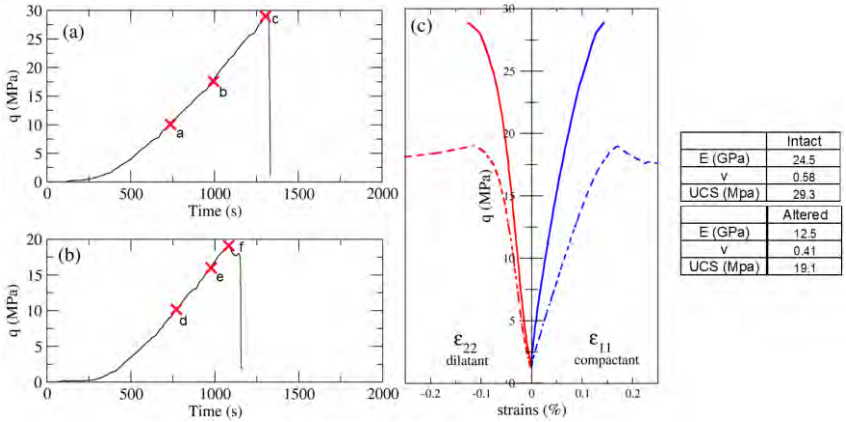

	Intact
E (GPa)	24.5
v	0.58
UCS (Mpa)	29.3

	Altered
E (GPa)	12.5
v	0.41
UCS (Mpa)	19.1

Figure 7 : Loading curves of (a) intact and (b) 6 RAT macroscopic samples and (c) Stress-strain curves inferred from DIC calculation on the whole surface of the samples. Elastic Moduli and USC are reported in the table

Fig. 7(a,b) presents time-load curves with larger UCS for unaltered than altered sample, in agreement with the results presented further in Fig. 6. Red crosses on the curves correspond to the images presented in Fig. 8 and 9. Fig. 7(c) is obtained by DIC computing the strain on the all observation surface. From this analysis, Young's moduli are comparable with those previously obtained by classical uniaxial tests, but the Poisson's ratios are not. The latter discrepancy may be explained by a global displacement of the sample toward the camera (due to sample sliding) which is falsely interpreted as dilation effect and results in an overestimation of the radial deformation.

Optical Results

Fig. 8 presents the in-plane strains ε_{11} and ε_{22} for intact and altered samples at three different stages of loading. At 10.1 MPa, the intact sample (ε_{11} ~ -0.02%) showed a small mean deformation (ε_{11} ~ -0.02%) expressed by a light blue color. At 17.6 MPa, equivalent to ε_{11} ~ -0.05%, some spots presented higher deformation levels, seemingly at random. Finally at 29.0 MPa, tensile cracks developed linking the previously noticed spots. Conversely, the altered samples at a similar stress level (10.2 MPa) presented a larger mean strain (ε_{11} ~ -0.06%) represented by deep blue hue, indicating a more compressive behavior. At 16.0 MPa (ε_{11} ~ -0.12%), the top right area exhibits larger strain, characterized by a strong localization, initiating the final failure pattern at 19.1 MPa.

In conclusion, the two kinds of samples presented contrasting deformation patterns. The intact one developed progressively a interconnected network of shear bands leading to the development of diffuse micro damages until the peak stress. Conversely the altered one presented a higher mean compressibility, but also very strong localization in a few areas which trigger local instabilities. The reason for these localizations remains unclear at this scale and requires micromechanical investigations at the scale of microstructure, as shown in the next section.

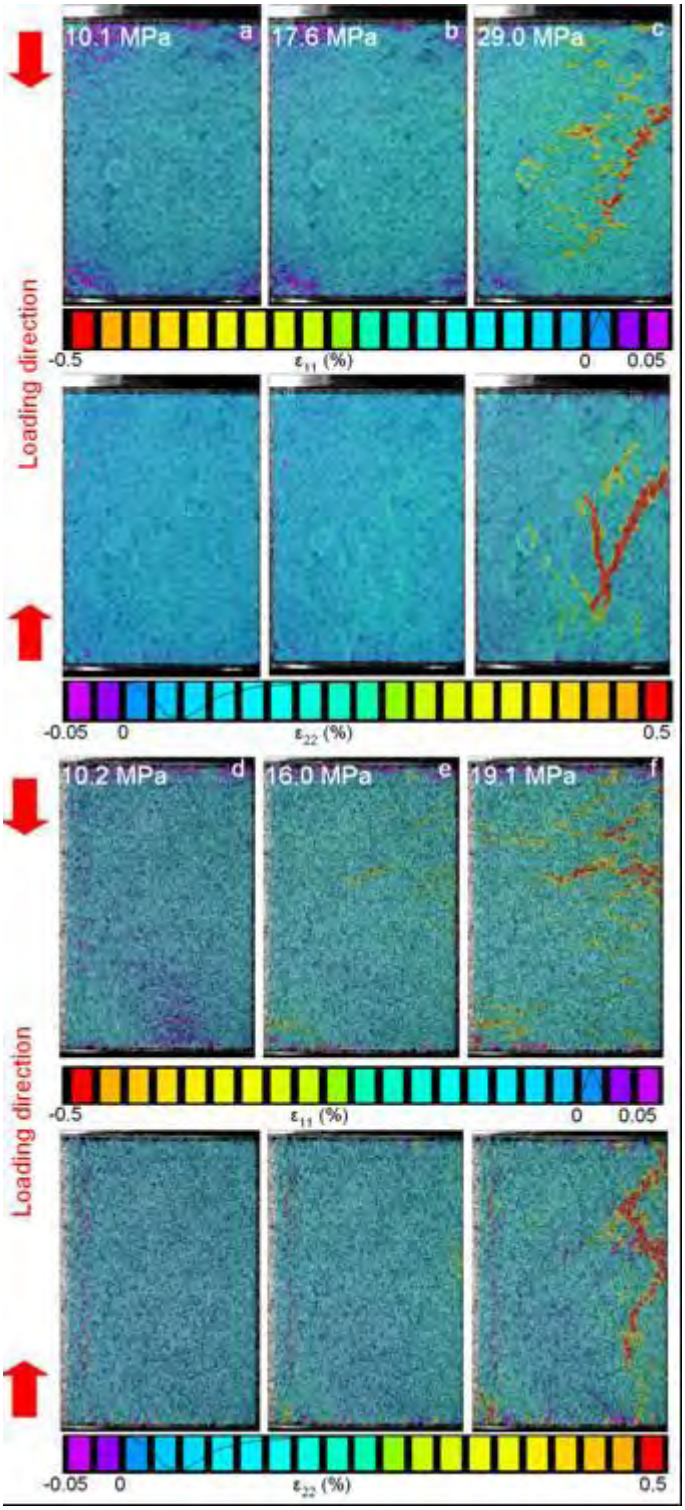

Figure 8 : In-plane strain components ε_{11} and ε_{22} maps for (a, b, c) intact sample and for (d, e, f) 6 RATs sample, at loading stages reported on the Fig. 7 (grid size: 2813 x 4583 pixels, measurements basis 56 pixels = 424µm)

Fine Scale Effects Of The Alteration

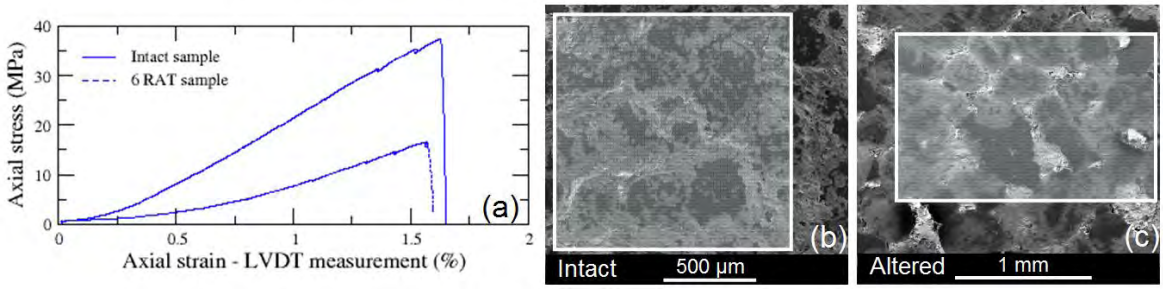

Figure 9 : (a) Stress-strain curves obtained on intact and 6 RATs small sample in the SEM, examples of (b) intact sample and (c) 6 RATs sample reference images acquired at magnification x60 and x80, respectively. The white areas correspond to reference grids

Fig. 9 presents the results of uniaxial loading in the SEM chamber for an intact and a 6 RAT sample. The axial strain value on the loading curves were certainly overestimated because the LVDT takes into account the compliance of the whole compressive rig. Nevertheless, the altered sample were clearly weaker than the intact one.

SEM Results On Intact Samples

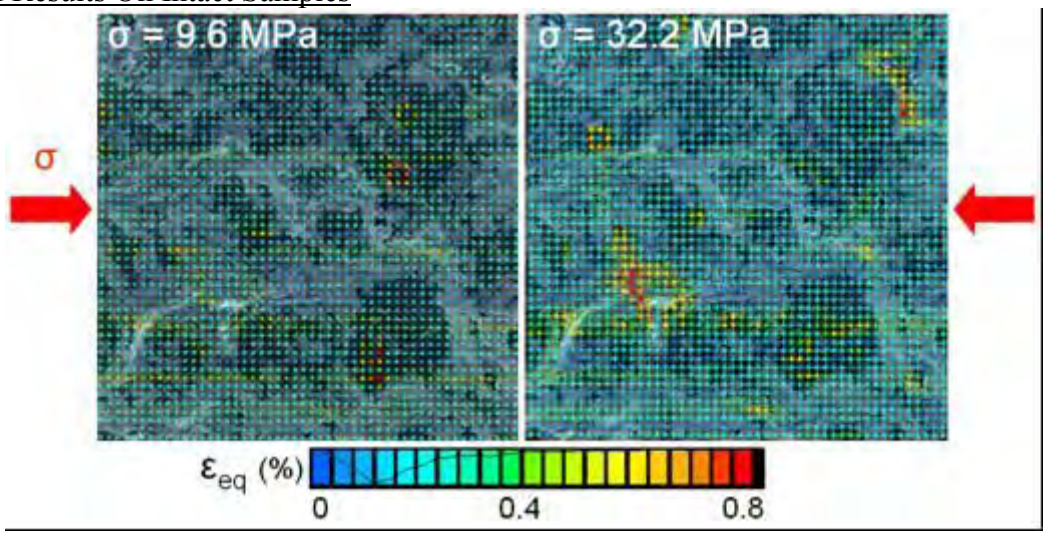

Figure 10 : Equivalent deformation maps of intact sample at two steps of loading, the reference image is reported on the Fig. 9(b) (grid size : 3100 x 3046 pixels and measurements basis of 18 µm)

Fig. 10 presents an equivalent deformation map, characteristic of the mechanical behavior of the intact sample. The observed deformation corresponded to closure of porosity (micro damage). Failure were sudden without precursor signs. These observations are in agreement with the results of optical DIC (Fig. 7). Indeed, except for the localization in porosity, the mean deformation of the area were similar to the mean deformation observed in Optical DIC (~0.2%). At this scale, we did not see obvious cracking which is also in

agreement with Optical DIC observations, where the development of a tensile crack network happens at a larger scale.

SEM Results On Altered Samples

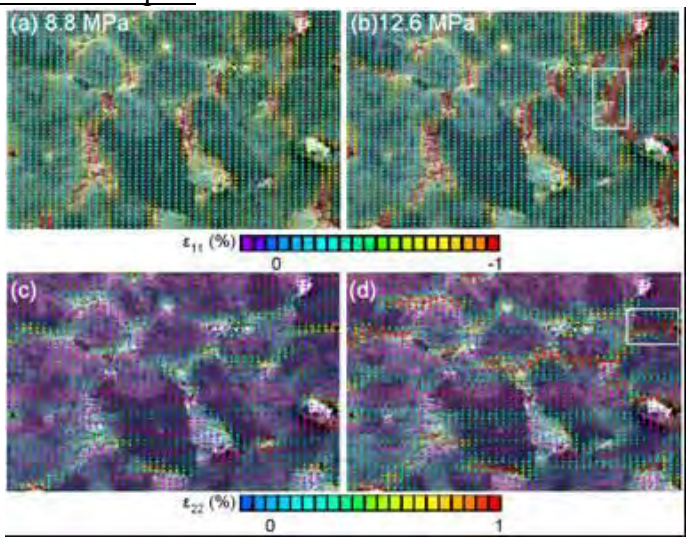

Figure 11 : In-plane strain components (a, b) ε_{11} and (c, d) ε_{22} maps of 6 RATs sample at two steps of loading, the reference image is reported on Fig. 9(c) (grid size : 3452 x 1899 pixels, measurements basis of 29 µm)

Fig. 11 presents ε_{11} and ε_{22} maps for altered sample at 8.8 MPa and 12.6 MPa. The main results were the early appearance of microcracks, as well as porosity closure. Besides tensile microcracking visible on ε_{22} maps (located in the white rectangle in Fig. 11(d)), we also observed apparently compressive localizations on ε_{11} maps (located in the white rectangle in Fig. 11(b)), which actually represents grain overlapping.

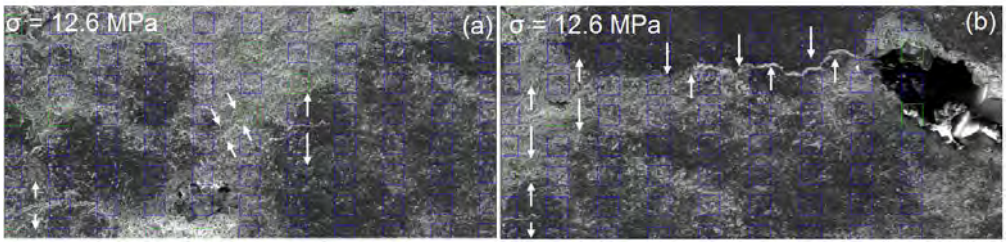

Figure 12 : (a) Extensive and compressive cracks and (b) Extensive cracks developed at grain interface, white arrow directions highlight the opening or closure of cracks.

Microcracks initiated and developed at grain interfaces (Fig. 12(f)) or in the grains (Fig. 12(e)). This type of continuous strain accommodation is consistent with optical results and can explain the lower resistance of the altered sample and the more diffuse accommodation at macro scale.

5 – CONCLUSIONS

We have altered carbonate reservoir rock. We have observed hydromechanical evolutions, which are clearly related to microstructural changes. The DIC allows us to better understand how global damage mechanisms relate to the local microstructural evolutions

of altered samples. At the macroscale, for the intact sample, an almost homogeneous deformation is observed followed by sudden failure at the peak stress. The altered samples sustain higher deformation levels and exhibit successive strain localization events. At the microscale, for the intact sample, the deformation is mostly accommodated within the inter-granular pores. In contrast, the altered samples show a gradual damage characterized by nucleation of microcracks at the grain contacts and their propagation within the grains. DIC results suggest that the dissolution of solid phases increases the local heterogeneities of the samples, leading to strain localization and mechanical weakening.

ACKNOWLEDGEMENTS
This work is co-funded by IFPEN and LMS. At IFPEN, we thank J. Guelard, J.M. Nez, M.-C. Lynch and L. Monmusson for technical assistance with the acidizing experimental set-up and the petrophysical and mechanical characterizations. At LMS, we thank E. Héripré and D. Yang for assistance with the optical and SEM compression set-ups.

BIBLIOGRAPHY

[1] André, L., P. Audigane, M. Azaroual, , and A. Menjoz. "Numerical modeling of fluid–rock chemical interactions at the supercritical CO2–liquid interface during CO2 injection into a carbonate reservoir, the Dogger aquifer (Paris Basin, France)". *Energy Conversion and Management*, (2007) **48**(6), p.1782-1797.
[2] Le Guen, Y., R. Hellmann, M. Collombet, J.-P. Gratier, E. Brosse, and I. Fran. "Enhanced deformation of limestone and sandstone in the presence of high P CO2 fluids". *Earth*, (2007) 112.
[3] Bazin, B. "From matrix acidizing to acid fracturing: A laboratory evaluation of acid/rock interactions". *Old Production & Facilities*, **16**(1), p. 22–29.
[4] Noiriel, C. "Investigation of porosity and permeability effects from microstructure changes during limestone dissolution". *Geophysical Research Letters*, (2004), **31**(24), p.2-5.
[5] Egermann, P., E. Bemer, and B. Zinszner. "An experimental investigation of the rock properties evolution associated to different levels of CO2 injection like alteration processes". Paper SCA 2006-34*, Proceeding of the international Symposium of the Society of core Analysts,* Trondheim, Norway, (2006) p. 12-16.
[6] Bemer, E., and J. M. Lombard. (2009). From Injectivity to Integrity Studies of CO 2 Geological Storage. *Oil & Gas Science and Technology – Revue de l'Institut Français du Pétrole*, (2001) ***65***(3), p. 445-459.
[7] Gourri, A. "Contribution à l'étude de l'influence des conditions de drainage sur les propriétés poroélastiques des roches carbonatées". PhD study (1991), Grenoble 1, France.
[8] Anselmetti, F.S., and G.P, Eberli. "Controls on sonic velocity in carbonates". *Pure and Applied Geophysics,*(1993) **141**(2-4), p. 287-323.
[9] Dautriat, J., M. Bornert, N. Gland, A. Dimanov, and J. Raphanel. "Localized deformation induced by heterogeneities in porous carbonate analysed by multi-scale digital image correlation". *Tectonophysics*, (2011) **503**(1-2), p. 100-116.
[10] Zhu, W. and T.-F. Wong. "The transition from brittle faulting to cataclastic flow: Permeability evolution" *Journal of Geophysical Research*. (1997) **102**(B2), p. 3027-3041.
[11] Allais L., Bornert M., Bretheau T. amd Caldemaison D., 'Experimental characterisation of the local strain field in a heterogeneous elastoplastic material', *Acta. Mettal. Mater*, **42**, 1994.
[12] Doumalin P., Bornert M. and Caldemaison D., 'Microextensometry by DIC applied to micromechanical studies using SEM', *Proc. Int. Conf. Adv. Techn. Exp. Mech.*, 1999.